Supporting Information

Vilarrasa and Carrera 10.1073/pnas.1413284112

SI Text

Effective Stress Data. We have compiled effective stress data of both sedimentary and crystalline rocks (Fig. 1). Unlike hard crystalline rocks, the softer sedimentary rocks are usually noncritically stressed. The data displayed in Fig. 1 is detailed in Table S1.

Model of the Upper Crust. To test whether sedimentary formations are likely to become critically stressed or not, we built a model of the upper crust to simulate the stress buildup induced by the strain of plate tectonics (Fig. S1). We impose a strain rate typical of plate tectonics, i.e., 10^{-17} s^{-1} (1) at the left boundary of the model. As a result of this strain, the upper crust, which we consider that its initial stress state is isotropic, will undergo an increase of the horizontal stresses. Apart from the isotropic stress state, the initial conditions are hydrostatic pressure and a geothermal gradient of 30 °C/km, with a surface temperature of 10 °C. Both the pressure and temperature are maintained constant throughout the simulation. In this model, we consider that the shallower 2.5 km are sedimentary rocks and below them, there is the crystalline basement.

We assume that our model of the upper crust behaves elastically. We deem that this rheology is appropriate because the elastic plate thickness is usually thicker than the 16 km considered in our model (1–3). The stiffness of the rocks is a function of depth and of the rock type. We chose the stiffness of the sedimentary rocks to be in agreement with the compressibility values given by Neuzil (4) for sedimentary rocks (Fig. S2). The stiffness of the crystalline basement is based on values given by Brudy et al. (5) for the gneiss at the deep well KTB, Germany. We assume that the stiffness increases with depth and that the upper part of the crystalline basement is softer than the deeper part because it could have been exposed to alteration (6). The resulting vertical profile of the Young's modulus as a function of depth is shown in Fig. S3.

Despite the simplicity of the model, it illustrates the concept that sedimentary rocks, which are softer than the crystalline basement, become less stressed than the crystalline basement. We solve this thermo-hydro-mechanical problem using the finite element code CODE_BRIGHT (7, 8). The model is discretized with structured quadrilateral elements. The mesh is regular, with an element size of 2 km in the horizontal direction and 100 m and 500 m in the vertical direction for the sedimentary rocks and the crystalline basement, respectively. We have ensured that further refinement of the mesh does not affect the results.

Model of CO_2 Injection. For studying the overpressure and caprock stability evolution as a result of CO_2 injection, we consider an idealized horizontal reservoir overlaid and underlain by a low-permeability and high entry pressure formation (Fig. S4). The reservoir thickness is of 50 m and the thickness of the seals on top and below of the reservoir is 100 m. The top of the reservoir is placed at a depth of 1,500 m. The model is completed by an upper aquifer that extends up to 500-m depth and by a basal aquifer that reaches a depth of 2,500 m. We assume that the upper 500-m-thick overburden has such a low shear stiffness that it does not need to be included in the model. To avoid boundary effects on the hydromechanical behavior of the model, the model extends laterally 100 km. The model is axisymmetric to represent a vertical well, which has a radius of 0.15 m.

The hydromechanical properties of the rocks that form the model are listed in Tables S2 and S3. Table S2 displays the values of the base case, and Table S3 includes reasonable ranges of values of the stiffness and the porosity of the rocks. The reservoir corresponds to a permeable limestone and the seals to a shale (9). The upper and basal aquifers have the same hydraulic properties, but the basal aquifer is stiffer because of its higher confining pressure.

The initial conditions are hydrostatic pressure and a constant temperature of 60 °C, which corresponds to the mean temperature of the reservoir. We assume isothermal conditions and that both horizontal stresses are equal. The initial stress field displays a relationship between horizontal and vertical effective stresses of $\sigma'_{h_0} = 0.5\sigma'_{v_0}$, where σ'_{h_0} is the initial horizontal effective stress, $\sigma'_{v_0} = 0.013z$ MPa is the initial vertical effective stress and z is depth. This relationship between the vertical and the horizontal effective stresses is equivalent to a mobilized friction coefficient of 0.35, which is in the lower limit of the friction coefficients of sedimentary rocks of CO_2 storage sites (Table S1). As a first step, a steady-state calculation is carried out to ensure consistent initial conditions in equilibrium for the pressure and stress fields.

The hydraulic boundary conditions are constant hydrostatic pressure at the outer boundary and no flow at the other boundaries. At the injection well, a mass flow rate of 2 Mt/y of CO_2 is uniformly injected along the whole thickness of the reservoir for 2,000 d. As for the mechanical boundary conditions, we apply a constant lithostatic stress on the upper boundary and no displacement perpendicular to the other boundaries.

The hydromechanical response of the rocks to CO_2 injection in a deep saline reservoir is modeled using the fully coupled finite element numerical code CODE_BRIGHT (7, 8), which was extended to simulate CO_2 injection by Vilarrasa et al. (10). The model is discretized with structured quadrilateral elements. The mesh is finer close to the injection well in the reservoir and seals and becomes coarser further away. We have ensured that further refinement of the mesh does not change the results.

We discuss here the sensitivity of overpressure evolution to variations of Young's modulus and porosity within the ranges of Table S3 (Fig. S5). Overpressure is virtually insensitive to changes in the stiffness and porosity of the upper and basal aquifers and to the porosity of the caprock. However, caprock stiffness does affect overpressure, because it affects the storativity of the reservoir (11). Stiff caprocks reduce the effective storage coefficient of the reservoir and therefore, pressure buildup is higher than for soft caprocks. Similarly, stiff reservoirs yield a higher overpressure than soft reservoirs. Finally, high porosity reservoirs induce a higher overpressure than low porosity reservoirs. This may seem paradoxical, but reflects that permeability has not been changed. A small porosity implies that the CO_2 plume is large, which will cause a low overpressure because CO_2 viscosity is small, which reduces the overall resistance to flow.

CO_2 Dissolution Calculations. Dissolution is sensitive to two factors: resident volume of water (porosity, ϕ, times thickness, b) and vertical permeability, k. Dissolution may also be affected by aquifer bottom slope, as the dense CO_2 rich brine will tend to sink downslope, but this effect is neglected here. Permeability controls the dissolution rate, m, whereas the resident volume controls the maximum dissolution capacity, M. Both M and m are proportional to CO_2 solubility, χ. The maximum dissolution capacity is given by

$$M = \phi b \rho \chi \qquad \text{[S1]}$$

where ρ is water density. The solubility is highly sensitive to pressure, temperature and brine salinity. Pool et al. (12) provide

values of solubility (mass fraction) for 0.5 M water (salinity comparable to that of seawater) that range from 4.1% (100 bars, 55 °C) to 5.5% (200 bars, 30 °C, corresponding to cold CO_2 injection or storage below the ocean). Adopting a storage formation with b = 100 m, ϕ = 0.1, ρ = 1,000 kg/m^3, and χ = 0.049, the maximum dissolution capacity results in M = 0.49 Mt/km^2, or a capacity of 19.6 Mt for a 40 km^2 CO_2 plume, which suggests that storage capacity for dissolved CO_2 is significant in deep saline formations.

Different expressions have been derived for the dissolution rate (13, 14). Expressed in the same form, they can be written as

$$m = \alpha\chi\rho u_b, \qquad u_b = k\varepsilon\rho g/\mu, \qquad \text{[S2]}$$

where u_b is the flux of a dense fluid sinking in a light fluid when the density difference is $\Delta\rho$, g is gravity, μ is water viscosity and $\varepsilon(\Delta\rho/\rho)$ is the buoyancy factor. Pool et al. (12) also provide values for this factor, which ranges around 0.8–1.6%, for the conditions adopted for solubility above. The factor α was numerically evaluated as 0.0175 by Pau et al. (14) and as 0.0142 by Hidalgo and Carrera (13).

It is clear that the critical factor in the evaluation of m is the vertical permeability. If χ = 0.49, ε = 0.012, $\mu = 5.9 \cdot 10^{-4}$ Pa·s, and $k = 2 \cdot 10^{-12}$ m^2, then m = 0.01 Mt/y/km^2, or 0.4 Mt/y for a 40-km^2 plume, which is significant. For example, if we analyze a storage site with a high permeability as Sleipner, where the CO_2 plume extends 12 km^2 after having injected 12 Mt of CO_2 in 12 y (15), the dissolution rate would be of 0.12 Mt/y, which is a 12% of the injection rate. Obviously, the dissolution rate would drop to $5{\cdot}10^{-4}$ Mt/y/km^2 if $k = 10^{-13}$ m^2, which is negligible and supports the generalized perception that dissolution is only relevant over long periods of time.

1. Zoback MD, Townend J, Grollimund B (2002) Steady-state failure equilibrium and deformation of intraplate lithosphere. *Int Geol Rev* 44:383–401.
2. McNutt MK, Diament M, Kogan MG (1988) Variations of elastic plate thickness at continental thrust belts. *J Geophys Res* 93:8825–8838.
3. Handy MR, Brun J-P (2004) Seismicity, structure and strength of the continental lithosphere. *Earth Planet Sci Lett* 223:427–441.
4. Neuzil CE (1986) Groundwater flow in low-permeability environments. *Water Resour Res* 22(8):1163–1195.
5. Brudy M, Zoback MD, Fuchs K, Rummel F, Baumgärtner J (1997) Estimation of the complete stress tensor to 8 km depth in the KTB scientific drill holes: Implications for crustal strength. *J Geophys Res* 102(B8):18453–18475.
6. Christensen NI, Mooney WD (1995) Seismic velocity structure and composition of the continental crust: A global view. *J Geophys Res* 100:9761–9788.
7. Olivella S, Carrera J, Gens A, Alonso EE (1994) Non-isothermal multiphase flow of brine and gas through saline media. *Transp Porous Media* 15:271–293.
8. Olivella S, Gens A, Carrera J, Alonso EE (1996) Numerical formulation for a simulator (CODE_BRIGHT) for the coupled analysis of saline media. *Eng. Computations* 13:87–112.
9. Vilarrasa V (2014) Impact of CO_2 injection through horizontal and vertical wells on the caprock mechanical stability. *Int J Rock Mech Min Sci* 66:151–159.
10. Vilarrasa V, Bolster D, Olivella S, Carrera J (2010) Coupled hydromechanical modeling of CO_2 sequestration in deep saline aquifers. *Int J Greenh Gas Control* 4:910–919.
11. Vilarrasa V, Carrera J, Olivella S (2013) Hydromechanical characterization of CO_2 injection sites. *Int J Greenh Gas Control* 19:665–677.
12. Pool M, Carrera J, Vilarrasa V, Silva O, Ayora C (2013) Dynamics and design of systems of injecting dissolved CO_2. *Adv Water Resour* 62:533–542.
13. Hidalgo JJ, Carrera J (2009) Effect of dispersion on the onset of convection during CO_2 sequestration. *J Fluid Mech* 640:441–452.
14. Pau GSH, et al. (2010) High resolution simulation and characterization of density-driven flow in CO_2 storage in saline aquifers. *Adv Water Resour* 33(4):443–455.
15. Boait F, White N, Chadwick A, Noy D, Bickle M (2011) Layer spreading and dimming within the CO_2 plume at the Sleipner Field in the North Sea. *Energy Procedia* 4: 3254–3261.

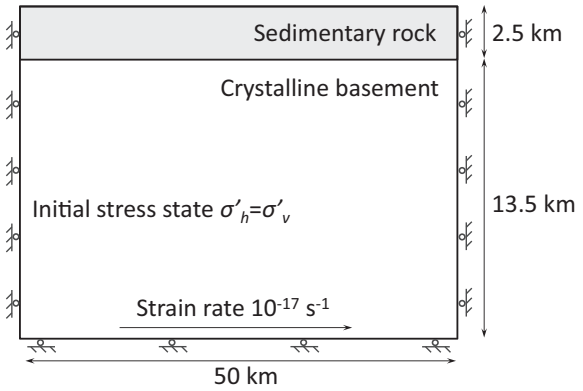

Fig. S1. Schematic representation of the upper crust model (not to scale). The upper 2.5 km represent sedimentary rocks, and the lower 13.5 km characterize the crystalline basement. The initial stress state is isotropic, but the horizontal stresses increase with time as a result of the strain rate typical of plate tectonics.

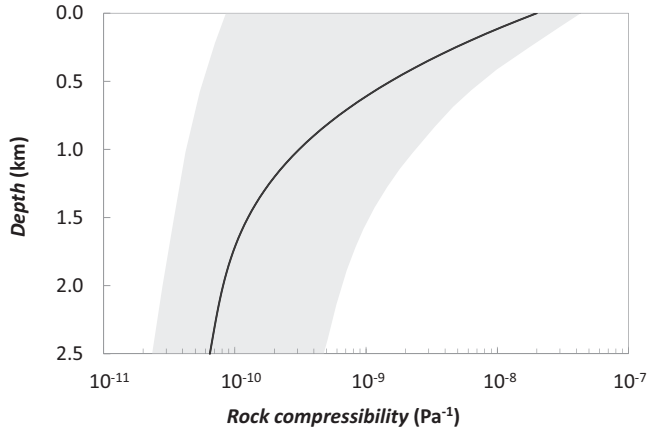

Fig. S2. Rock compressibility of the sedimentary rocks considered in our study. The shaded region indicates the range of compressibility of sedimentary rocks given by Neuzil (1).

1. Neuzil CE (1986) Groundwater flow in low-permeability environments. *Water Resour Res* 22(8):1163–1195.

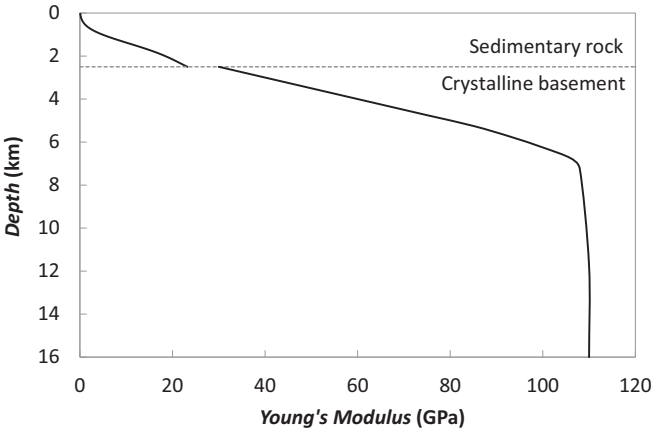

Fig. S3. Young's modulus as a function of depth of the sedimentary and crystalline rocks considered in the upper crust model. The sedimentary rocks are softer that the crystalline basement.

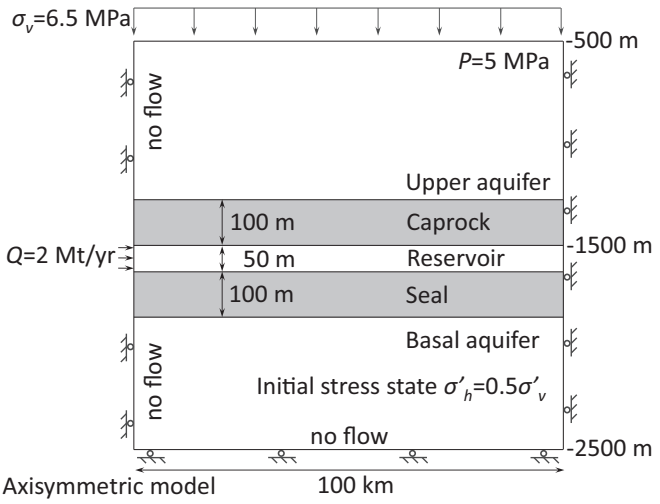

Fig. S4. Schematic representation of the CO_2 injection model (not to scale). 2 Mt/y of CO_2 are injected through a vertical well in a 50-m-thick reservoir overlaid and underlain by a seal.

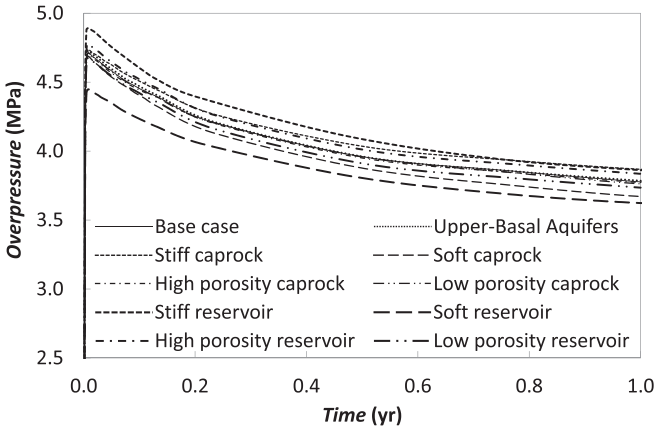

Fig. S5. Effect of subsurface heterogeneity on overpressure evolution.

Table S1. Effective stress data of sedimentary and crystalline rocks shown in Fig. 1

Site	Depth, m	σ'_1, MPa	σ'_3, MPa	μ, -	References
Sedimentary rocks of CO_2 storage sites					
In Salah, Algeria	1,800	31.7	12.6	0.48	Morris et al. (1)
Otway, Australia	2,000	49.4	22.4	0.41	Nelson et al. (2); Vidal-Gilbert et al. (3)
Snohvit, Norway	2,683	36	14	0.49	Chiaramonte et al. (4)
St. Lawrence Lowland, Canada	1,200	36.2	12.8	0.54	Konstantinovskaya et al. (5)
Tomakomai, Japan	2,352	20.1	10.1	0.35	Kano et al. (6)
Weyburn, Canada	1,450	19.5	11.5	0.50	White and Johnson (7)
Sedimentary rocks					
Allegany Co., New York	510	14.4	8.9	0.24	Haimson (8)
Bure argillite, France	500	9.5	7.0	0.15	Gunzburger (9)
Caddo-Pine Island, Louisiana	425	5.8	3.3	0.29	Haimson (8)
Dogger Limestone, France	600	9.5	3.0	0.61	Gunzburger (9)
Green River Basin, Wyoming	2,775	53.8	24.3	0.41	Haimson (8)
Henderson Project, Colorado	785	26.0	14.7	0.29	McGarr and Gay (10)
Henderson Project, Colorado	1,131	29.4	10.7	0.53	McGarr and Gay (10)
Hocking Co., Ohio	810	20.4	7.4	0.53	Haimson (8)
Ithaca, Michigan	1,230	38.2	17.2	0.41	Haimson (8)
Ithaca, Michigan	3,660	58.4	27.9	0.38	Haimson (8)
Ithaca, Michigan	5,110	95.9	44.9	0.39	Haimson (8)
Meeker, Colorado	470	7.3	3.8	0.33	Haimson (8)
Michigan Basin, Michigan	1,230	35.7	17.2	0.37	McGarr and Gay (10)
Michigan Basin, Michigan	2,806	42.1	13.9	0.58	McGarr and Gay (10)
Michigan Basin, Michigan	3,660	54.9	30.4	0.30	McGarr and Gay (10)
Michigan Basin, Michigan	5,110	83.9	43.9	0.33	McGarr and Gay (10)
Oxfordian limestone, France	400	10.5	4.0	0.5	Gunzburger (9)
Piceance Basin, Colorado	453	5.7	2.6	0.41	McGarr and Gay (10)
Rangely, Colorado	1,914	39.9	12.3	0.62	McGarr and Gay (10)
South of Vernal, Utah	2,750	37.5	24.0	0.23	McGarr and Gay (10)
Yucca Mountains, Nevada	250	5.7	2.9	0.34	Rutqvist et al. (11)
Crystalline rocks					
Basel, Switzerland	4,900	111.0	35.0	0.61	Häring et al. (12)
Copperton, Cape Province, South Africa	410	8.9	2.3	0.73	McGarr and Gay (10)
Dinkey Creek, California	325	6.8	2.3	0.58	Haimson (8)
Elliot Lake, Canada	700	30.0	10.0	0.58	McGarr and Gay (10)
Evander, Transvaal, South Africa	1,577	33.7	10.6	0.61	McGarr and Gay (10)
KTB, Germany	1,000	43.0	18.0	0.45	Brudy et al. (13)
KTB, Germany	3,000	73.0	23.0	0.61	Brudy et al. (13)
Le Mayet de Montagne, France	750	12.5	4.3	0.56	Cornet and Jianmin (14)
Montello, Wisconsin	190	14.1	3.1	0.83	Haimson (8)
Roodepoort, Transvaal, South Africa	2,300	47.0	16.0	0.57	McGarr and Gay (10)
Salem, South Carolina	120	7.8	1.8	0.80	Haimson (8)
Silver Summit Mine, Idaho	1,670	88.4	20.8	0.79	McGarr and Gay (10)
Sudbury Basin, Canada	2,134	58.2	16.1	0.69	McGarr and Gay (10)
Timmins, Canada	853	53.0	17.2	0.59	McGarr and Gay (10)
Valles Caldera, New Mexico	2,925	46.8	9.8	0.87	Haimson (8)

σ'_1 is the maximum effective stress, σ'_3 is the minimum effective stress and μ is the mobilized friction coefficient. -, no units.

1. Morris JP, Hao Y, Foxall W, McNab W (2011) A study of injection-induced mechanical deformation at the In Salah CO_2 storage project. *Int J Greenh Gas Control* 5(2):270–280.
2. Nelson E, Hillis R, Sandiford M, Reynolds S, Mildren S (2006) Present-day state-of-stress of southeast Australia. *APPEA J* 46(1):283–305.
3. Vidal-Gilbert S, et al. (2010) Geomechanical analysis of the Naylor Field, Otway Basin, Australia: Implications for CO_2 injection and storage. *Int J Greenh Gas Control* 4(5):827–839.
4. Chiaramonte L, White JA, Hao Y, Ringrose P (2013) Probabilistic Risk Assessment of Mechanical Deformation due to CO_2 Injection in a Compartmentalized Reservoir. *47th US Rock Mechanics/Geomechanics Symposium* (American Rock Mechanics Association, Alexandria, VA).
5. Konstantinovskaya E, Malo M, Castillo DA (2012) Present-day stress analysis of the St. Lawrence Lowlands sedimentary basin (Canada) and implications for caprock integrity during CO_2 injection operations. *Tectonophysics* 518:119–137.
6. Kano Y, et al. (2013) Fault stability analysis related to CO_2 injection at Tomakomai, Hokkaido, Japan. *Energy Procedia* 37:4946–4953.
7. White DJ, Johnson JW (2009) Integrated geophysical and geochemical research programs of the IEA GHG Weyburn-Midale CO_2 monitoring and storage project. *Energy Procedia* 1(1): 2349–2356.
8. Haimson BC (1977) Crustal stress in the continental United States as derived from hydrofracturing tests. *Geophysical Monograph Series* 20:576–592.
9. Gunzburger Y (2010) Stress state interpretation in light of pressure-solution creep: Numerical modelling of limestone in the Eastern Paris Basin, France. *Tectonophysics* 483(3):377–389.
10. McGarr A, Gay NC (1978) State of stress in the earth's crust. *Annu Rev Earth Planet Sci* 6:405–436.
11. Rutqvist J, Freifeld B, Min KB, Elsworth D, Tsang Y (2008) Analysis of thermally induced changes in fractured rock permeability during 8 years of heating and cooling at the Yucca Mountain Drift Scale Test. *Int J Rock Mech Min Sci* 45(8):1373–1389.
12. Häring MO, Schanz U, Ladner F, Dyer BC (2008) Characterization of the Basel 1 enhanced geothermal system. *Geothermics* 37:469–495.
13. Brudy M, Zoback MD, Fuchs K, Rummel F, Baumgärtner J (1997) Estimation of the complete stress tensor to 8 km depth in the KTB scientific drill holes: Implications for crustal strength. *J Geophys Res* 102(B8):18453–18475.
14. Cornet FH, Jianmin Y (1995) Analysis of induced seismicity for stress field determination and pore pressure mapping. *Pure Appl Geophys* 145:677–700.

Table S2. Properties of the rocks considered in the model (base case)

Property	Reservoir	Caprock and seal	Upper aquifer	Basal aquifer
Young's modulus, E, GPa	10	5	2.5	20
Poisson ratio, ν, -	0.3	0.3	0.3	0.3
Porosity, ϕ, -	0.1	0.01	0.1	0.1
Intrinsic permeability, k, m^2	10^{-13}	10^{-16}-10^{-20}	10^{-14}	10^{-14}
Relative liquid permeability, k_{rl}, -	S_l^3	S_l^6	S_l^3	S_l^3
Relative gas permeability, k_{rg}, -	S_g^3	S_g^6	S_g^3	S_g^3
Gas entry pressure, P_0, MPa	0.02	1.0	0.02	0.02
Van Genuchten shape parameter, m, -	0.8	0.3	0.8	0.8

-, no dimensions.

Table S3. Reasonable ranges of stiffness and porosity of the deep sedimentary rocks considered in the model

Property	Reservoir	Caprock and seal	Upper aquifer	Basal aquifer
Young's modulus, E, GPa	5–20	2.5–10	1–5	10–25
Porosity, ϕ, -	0.05–0.3	0.005–0.05	0.05–0.3	0.05–0.3

-, no dimensions.